Detailing the influence of PEO-coated biodegradable Mg-based implants on the lacuno-canalicular network in sheep bone: A pilot study

Jonathan Espiritu [a],[*], Sandra Sefa [b], Hanna Ćwieka [b], Imke Greving [c], Silja Flenner [c], Regine Willumeit-Römer [b], Jan-Marten Seitz [a], Berit Zeller-Plumhoff [b],[**]

[a] *Syntellix AG, Hannover, Germany*
[b] *Institute of Metallic Biomaterials, Helmholtz-Zentrum Hereon, Geesthacht, Germany*
[c] *Institute of Materials Physics, Helmholtz-Zentrum Hereon, Geesthacht, Germany*

ARTICLE INFO

ABSTRACT

An increasing prevalence of bone-related injuries and aging geriatric populations continue to drive the orthopaedic implant market. A hierarchical analysis of bone remodelling after material implantation is necessary to better understand the relationship between implant and bone. Osteocytes, which are housed and communicate through the lacuno-canalicular network (LCN), are integral to bone health and remodelling processes. Therefore, it is essential to examine the framework of the LCN in response to implant materials or surface treatments.

Biodegradable materials offer an alternative solution to permanent implants, which may require revision or removal surgeries. Magnesium alloys have resurfaced as promising materials due to their bone-like properties and safe degradation *in vivo*. To further tailor their degradation capabilities, surface treatments such as plasma electrolytic oxidation (PEO) have demonstrated to slow degradation.

For the first time, the influence of a biodegradable material on the LCN is investigated by means of non-destructive 3D imaging. In this pilot study, we hypothesize noticeable variations in the LCN caused by altered chemical stimuli introduced by the PEO-coating.

Utilising synchrotron-based transmission X-ray microscopy, we have characterised morphological LCN differences around uncoated and PEO-coated WE43 screws implanted into sheep bone. Bone specimens were explanted after 4, 8, and 12 weeks and regions near the implant surface were prepared for imaging. Findings from this investigation indicate that the slower degradation of PEO-coated WE43 induces healthier lacunar shapes within the LCN. However, the stimuli perceived by the uncoated material with higher degradation rates induces a greater connected LCN better prepared for bone disturbance.

1. Introduction

An expanding market for new implants has been established as a response to an increase in orthopaedic surgeries. Surgical intervention requiring bone implants aim to create direct contact between implant material and bone. How this contact which is influenced by bone reorganization and remodelling is generally studied as well as a deeper understanding of bone healing around modern implant materials and technologies is unclear.

Bone is a hierarchical material that requires studying at several scales with each hierarchical level containing significant information.

Macro-to micro-scale investigations are conducted to study the bone-to-implant interface and bone volume to total volume in order to assess the overall osseointegration of the implant [1,2]. Scaling further to the nanoscale, the study and imaging of bone cell arrangement can be achieved [3]. The most abundant bone cell type [4], osteocytes, are dispersed throughout the mineralized extracellular matrix (ECM) and are critical to bone forming and remodelling processes [5]. Mature osteocytes are situated in a highly connected system named the lacuno-canalicular network (LCN). Entrapped in the lacunae, osteocytes are connected through dendritic channels called canaliculi in which they establish communication. Recently, canalicular junctions (CJ) have

shown to play a significant role in the LCN and have also been investigated [6]. The LCN enables biochemical signal communication between osteocytes and the transportation of nutrients [4]. Osteocytes locally initiate bone remodelling by generating signals in response to mechanical stimuli in the form of shear stress due to the flow of the extracellular fluid (ECF). Bone deformations are perceived by osteocytes and transduced into a signal which is transmitted to the rest of the network [7], triggering the recruitment of osteoblasts and osteoclast precursor cells [8]. Besides the mechanosensory capabilities of osteocytes, ECF found in the LCN enables mineral exchange with ECM [9]. Damage to the LCN or reduction in the LCN surface area may in turn impair mineral mobilisation and the mechanotransduction properties of osteocytes. Reduced interconnectivities hinder osteocyte communication and bone remodelling [10]. Irregular LCNs have been associated with bone diseases such as osteoporosis, osteoarthritis, and osteomalacia [11]. Furthermore, sex and age-related changes have been reported to show a decrease of lacunae density and loss of canaliculi, altering communication within the LCN [10,12]. Therefore, disruption to the LCN due to bone damage or implantation of (stimulating) biomaterials warrants further investigation.

Today, orthopaedic implants are used to replace or support damaged bone. However, traditional implant materials have shown to introduce unwarranted inflammatory responses [13] and further refracture risks [14]. Magnesium (Mg) and Mg-based alloys have re-emerged as promising alternative implant materials due to their successful degradation performance *in vivo* [15]. The similar elastic modulus and densities between Mg-based alloys and natural bone negate negative mechanical defects such as stress-shielding [16,17]. Though successful clinical cases have been reported using Mg-based alloys as implant material [18–22], additional research in potential surface treatments to further optimise degradation capabilities of Mg is on-going.

An inherent characteristic of pure Mg implants is fast degradation accompanied by hydrogen gas accumulation. This build-up of gas may lead to mechanical instability and consequently ineffective implantation. To overcome this, one surface treatment in particular, plasma electrolytic oxidation (PEO) has shown to lower the degradation rate of non-treated Mg-based implants [23–26]. Furthermore, PEO treatments surpass other surface technologies by producing thicker coatings, excellent adhesive strength, and can be applied to complex geometries [27]. By augmenting the degradation capabilities of these alloys further, Mg-based implants could potentially address other indications and fracture types which may require a more tailored degradation rate. Although there have been investigations of the LCN near permanent materials such as titanium [28], there is no documentation of LCN characterisation around biodegradable material.

Advancements in synchrotron-based imaging allows for better time effective imaging, without compromising imaging capabilities or sample damage. Characterising the structures found in the LCN has been challenging to date, as imaging requires a relatively large field-of-view and spatial resolutions below 100 nm. Human lacunae have previously been reported to have an average surface area of 20–70 μm^2 [29]. Canaliculi have been described to have an average diameter of 100–600 nm [30, 31], being much more difficult to resolve. Previously, the LCN has been characterised with various imaging modalities. (Quasi) two-dimensional methods including light [32], scanning electron [33–36], and transmission electron microscopy [30,37–39] have been utilised to image LCN structures though limited due to penetration depth and challenging sample preparation. Confocal microscopy [6,7,10,40,41] has also been applied, though with limited field-of-view. By comparison, X-ray and synchrotron radiation-based methods including ptychography, transmission X-ray microscopy (TXM) and near-field holotomography are enabling studying the LCN at high resolutions non-destructively in 3D with a relatively large field-of-view [3,6,9,42–47]. Though laboratory sources may provide similar spatial resolutions, synchrotron radiation increases imaging speed with comparable or better image quality [48]. In this investigation, synchrotron radiation-based X-rays are

conditioned by a double crystal monochromator and are further shaped by a condenser onto bone specimen. Behind the sample, Zernike phase rings are placed to attain qualitative phase contrast before images are captured with an X-ray camera.

In addition to the lack of LCN characterisation around degraded Mg-based implants, there is currently no information on the influence of PEO coating technologies on LCN morphology. As such, it is integral to understand the relationship between the PEO coating of Mg-based screws and the LCN to ensure successful implantation and controlled degradation. Two types of materials are analysed in this investigation, an untreated WE43-based magnesium alloy and a PEO surface-treated WE43-based magnesium alloy. The aim of this investigation is to provide a proof-of-concept study regarding the influence of PEO coatings on Mg-based screws implanted into sheep bone by characterizing the LCN at the nanoscale level in 3D using synchrotron radiation-based TXM. We hypothesize that the changed degradation rate induced by the PEO coating results in an altered chemical stimulus perceived by the LCN. This altered stimulus may lead to a change in LCN arrangement or morphology leading to variations in bone remodelling.

2. Materials and methods

2.1. Implant material

Orthopaedic interference screws (Fig. 1) with a diameter of 6 mm and 20 mm length were analysed in this investigation. Two types of materials manufactured by Syntellix AG (Hanover, Germany) were evaluated in this study: an untreated WE43-based magnesium alloy and a PEO surface-treated WE43-based magnesium alloy with a layer thickness of approximately 10–30 μm. Furthermore, the WE43 alloy is composed of Mg with the addition of Yttrium (3.7–4.3 %), Rare Earth Elements (2.4–4.4 %), and Zirconium (0.4 %) [49]. The specific composition and production methods for the alloy used in this investigation have been patented by Syntellix AG [50].

2.2. Animal experiments

Animal experiments were provided ethical clearance by the Landesamt für Arbeitsschutz, Verbraucherschutz und Gesundheit von Brandenburg (ethical clearance number 2347-31-2016). Bone specimens were explanted from the hind legs of three sheep (female German Heath, at least 2 years of age) with body weights between 43 and 57 kg. Each sheep received two screw implants, one made of WE43 and the other a
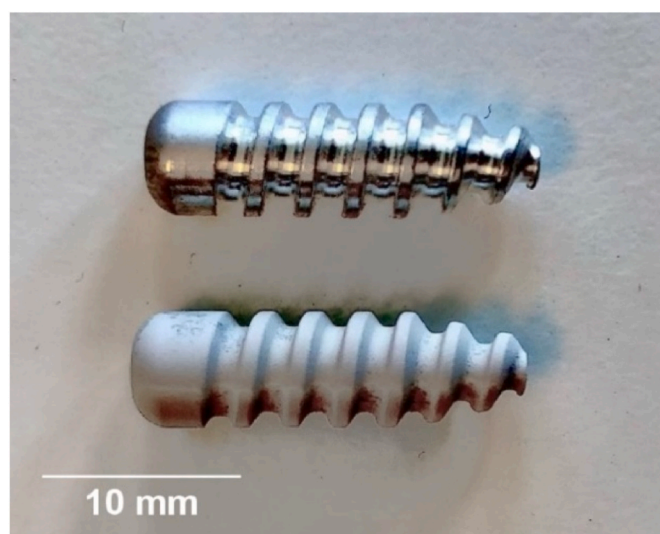

Fig. 1. Uncoated (top) and surface treated (bottom) WE43 orthopaedic interference screws manufactured by Syntellix AG (Hanover, Germany).

PEO-coated WE43 implant in either the distal femur or the proximal tibia. Implant material were spread among implant sites in such a manner that not only one specific material was placed in one site. The surgical methodology and selected time frames were chosen due to its acceptance for biological testing and evaluation of medical devices as set out by EN ISO 10993–6:2007 [51].

Before implantation, the animals were sedated intramuscularly with 0.4 mg/kg diazepam followed by general anaesthesia of 10 mg/kg ketamine. Shaving, cleaning, disinfection, and sterile covering of both knees took place before incisions. For tibial implantation, the skin was incised medial on the proximal end of the tibia exposing the shaft of tibia. The periosteum on the medial surface was then prepared. For femoral implantation, an incision was made medial on the distal end of the femur. The femoral trochlea and medial condyle were exposed and the caudomedial end of the trochlear crest was further prepared. At both implantation sites, a drill with 6 mm diameter was applied to a depth of approximately 20 mm. The application of interference screw was then achieved by means of screwdriver. Wounds were closed with continuous fascia and subcutaneous sutures, and with continuous intracutaneous suture skin bonding.

Butorphanol (0.5 mg/kg) was administered as prophylactic analgesia for a period of minimally three days *post operationem*. The animals were housed in groups during the acclimatization as well as during the study period. Individual times of postoperative recovery were ensured. Straw was used for bedding, supplied fresh and sufficiently on a weekly basis as well as if required. The sheep were provided with drinking water and ad libitum. After either four, eight, or twelve weeks of healing, the animals were sedated and put under general anaesthesia as described previously, followed by T61 intravenous euthanization.

2.3. Sample processing and data acquisition

Following euthanization, the implantation sites including the implanted screws were extirpated preserving adjacent bone tissue with at least 2 cm distance to the specific test item for a total of 6 explants. The samples were placed in increasing percentages of ethanol (Herbeta Arzneimittel Detlef Karlowski e.K., Berlin, Germany) for eight weeks. Following dehydration, the samples were embedded in polymethyl methacrylate (Kulzer GmBH, Hanau, Germany) and sliced in half along the length of the screw for further study.

2.3.1. Micro-computed tomography (μCT)

The embedded samples were first imaged via a laboratory μCT (Phoenix Nanotom by Baker Hughes, Celle, Germany) with an operating voltage of 100 kV at 70 μA current resulting in a pixel size of approximately 6 μm. Scanning was completed with 1000 ms exposure time with 2400 projections. Scans were reconstructed in Datos|x (Baker Hughes, Celle, Germany) where any movement during the scan was corrected using the image optimisation function. Imaging data acquired from μCT scans were then utilised for degradation rate calculations.

2.3.2. Scanning electron microscopy

Following μCT scanning, the embedded samples were cut perpendicular to the screw's long axis approximately 10 mm from the head of the screw using a diamond wire saw (Well Diamond Wire Saws SA, Mannheim, Germany) based on previous μCT scans. The exposed samples were then subject to polishing. Firstly, samples were cleaned with ethanol prior to and after mechanical polishing (Diamant suspension, with particle size 3 μm for 7 min). After cleaning, the quality of polishing was verified using a light microscope. The samples were then sputtered with gold for 1 min via a CRESSINGTON sputter coater (TESCAN GmbH, Dortmund, Germany). The sputtered samples underwent scanning electron microscopy (SEM). The TESASCAN AMBER X (TESCAN GmbH, Dortmund, Germany) was used to image the samples with a current of 10 pA and an applied voltage of 10 kV. A 300 μm field-of-view was achieved with an image size of 1024 pixels by 1024 pixels. Following

SEM imaging (Fig. 2), two regions of interest from the trabecular bone from each explant (millimetres from the screw surface) were selected for further processing. A further region was selected a larger distance from the screw surface to benchmark as undisturbed bone.

2.3.3. Synchrotron radiation-based transmission X-ray microscopy (TXM)

Bone specimens with a diameter and height of 50 μm were subject to focused ion beam milling at Fraunhofer Institute for Integrated Systems and Device Technology (Erlangen, Germany) producing a total of 18 samples (2 regions of interest approximately 150 μm from the bone-implant interface and 1 region at a distance of at least 1.3 mm per explant). The samples were mounted onto a custom holder. Following the milling process, imaging was performed at the nanotomography end station at the P05 imaging beamline operated by Helmholtz-Zentrum Hereon at the PETRA III storage ring at the Deutsches Elektronen-Synchrotron (Hamburg, Germany) [52]. An energy of 11.2 keV was selected using a Si111 double crystal monochromator ($\Delta E/E \sim 10^{-4}$). The sample was illuminated using a 1.8 mm beam shaping condenser with square fields of 50 μm by 50 μm, providing an illumination of the same size in the sample plane. The objective lens was a Fresnel zone plate with a diameter of 150 μm and an outermost zone width of 50 nm. Zernike phase rings were placed in the back-focal-plane of the Fresnel zone plate to enable phase contrast imaging. All optics were designed and fabricated in the X-ray Optics and Applications group of the Paul-Scherrer-Institut (Switzerland). The X-ray camera, a Hamamatsu C12849–101U camera with a sCMOS chip with 6.5 μm physical pixel size and a 10 μm Gadox scintillation layer, was placed 19.45 m behind the sample. With these optics, camera and distances, an effective field of view of roughly 46 μm with an effective pixel size of 22.8 nm was achieved. Image reconstruction was performed using respective TomoPy pipelines [53] with binning factor 2 of the raw images, resulting in a voxel size of 45.6 nm.

2.4. Degradation rate

μCT data was loaded into Fiji/ImageJ [54] for post-processing. Anistropic diffusion was applied to reduce noise before applying thresholding techniques to the data, segmenting the bone and implant material in Avizo (Version 2021.1, Thermo Fisher Scientific, Waltham, USA). Degradation rates were determined for both materials based on the segmented data using the following equation [55]:

$$Degradation\ rate = \frac{Initial\ volume\ of\ base\ material - corroded\ base\ volume}{Surface\ area\ of\ initial\ base \times time\ in\ years}$$

2.5. Calculation of lacunar density based on SEM images

SEM data underwent gaussian filtering within Fiji/ImageJ to prepare for segmentation and lacunae quantification. In Avizo, the implant was dilated by 1 mm and was subtracted from the original image to capture the region of interest. The bone within the region of interest was segmented by thresholding techniques to determine the surface area. After, the region of interest was exported from Avizo and loaded into Fiji/ImageJ where the multiple object selection tool was utilised to manually count the lacunae. Finally, the lacunar density was determined by dividing the counted lacunae by the surface are of bone which was previously segmented.

2.6. LCN segmentation

Before segmentation, the SRTXM data was first denoised by an iterative non-local means filter [56] designed to remove texture caused by back projected noise and artefacts in high resolution tomography. The denoised data was then subjected to segmentation in Avizo.

Firstly, the bone and LCN including the canaliculi, canalicular junctions, and lacunae structures were segmented using greyscale
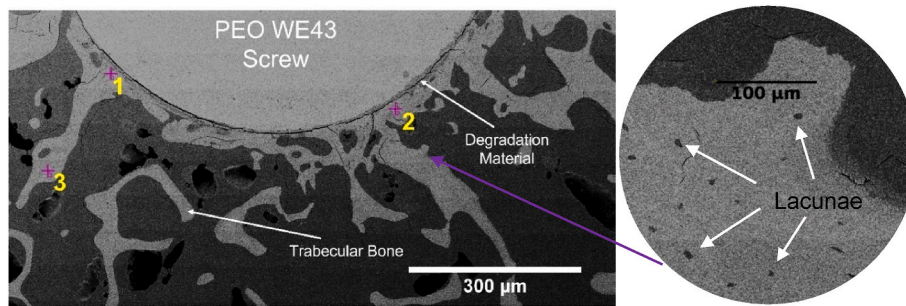
Fig. 2. Example cross section SEM image of PEO surface-treated screw samples after 12-weeks of implantation. Residual WE43 material, degradation layer, and trabecular sheep bone are visible. Two near regions (positions 1 and 2) and one further region (position 3) of interest are marked with crosses for milling. An example magnification of the SEM image showing lacunae is also shown (right), allowing for lacunar density to be derived from the image.

thresholding and manual correction. To segment the lacunae in Fig. 3, the LCN was masked and eroded to remove the canaliculi structures. The remaining structures were then labelled separately and were followed by volume size filtering to ensure only the lacunae were left and canalicular junctions were removed. Finally, the remaining objects were dilated to their approximate original shape followed by manual correction. To segment the canaliculi and canalicular junctions, the lacunae were subtracted from the LCN mask. Moreover, the LCN label was skeletonised for further nodal analysis.

2.7. Quantitative analysis of the LCN

Quantitative analysis was completed in Avizo. The lacunae were quantified by the number of lacunae found in the sample (Lc.N), the total volume of the lacunae (Lc.TV), the bone volume (BV), the density of the lacunae (Lc.N/BV) and the lacunar porosity (Lc.TV/BV). Additionally, the morphology of the lacunae was calculated in terms of sphericity and smoothness (or compactness) using the following equations:

$$Sphericity = \frac{\pi^{\frac{1}{3}}(6 \times Volume)^{\frac{2}{3}}}{Surface\ area}$$

$$Smoothness = \frac{Surface\ area^3}{36 \times \pi \times Volume^2}$$

The canaliculi were quantified by measuring the canalicular total volume (Ca.TV) and the canalicular porosity (Ca.TV/BV). To make better use of partially cut-off lacunae in the measured samples, the average number of canaliculi per lacunar surface area was also calculated. The canalicular junction density (CJ.N/BV) was determined by analysing the skeletonization nodes of the LCN. With the addition of lacunar volume, the total volume of the LCN (LCN.TV) and the LCN porosity (LCN.TV/BV) could be evaluated. Distance mapping was utilised in Avizo to calculate the distance between a matrix voxel and an LCN voxel (d_{LC}). Furthermore, the Fiji/ImageJ plugin [54], MorphoLibJ [57], was used to determine the average distance of any canalicular

point to the nearest lacunae (d_{net}) by means of geodesic distance mapping.

3. Results

3.1. Degradation rates

An example of a 3D rendered explant with segmented bone and screw material can be seen in Fig. 4 (A). At 4-weeks, the degraded PEO-coated screw shows good bone contact more noticeably at the tip. Calculated *in vivo* degradation rates for the uncoated and PEO-coated material are plotted for four, eight, and twelve weeks in Fig. 4 (B). Both samples revealed degradation rates lower than 1 mm/year during the first month, decreasing as time persists. Moreover, the PEO-coated material exhibited a more consistent and lesser degradation rate overall. There is approximately a 50% decrease in degradation rate initially, reducing to approximately 20% at 12 weeks between the two materials.

3.2. Qualitative comparison

Following μCT imaging, regions of interest within the bone surrounding the implant were identified for TXM in scanning electron microscopy (SEM) images of the same cross-section. Additionally, the lacunar density (Fig. 5) was calculated by segmenting the bone area imaged by SEM and manually counting the number of lacunae which were within 1 mm of the implant surface. The bone implanted with PEO material revealed to have approximately 30% lower lacunar density surrounding the implant when compared to the uncoated material.

Fig. 6 illustrates the image segmentation of the selected region of interests near the implant imaged using TXM organised by material and *in vivo* degradation time. The 3D renderings of segmented data show the lacunae (variously coloured) and canaliculi (light blue). From visual inspection, more lacunae were captured in the PEO samples. However, the lacunae found near the uncoated material appear larger in volume. There are clear differences in the organisation of canaliculi in terms of
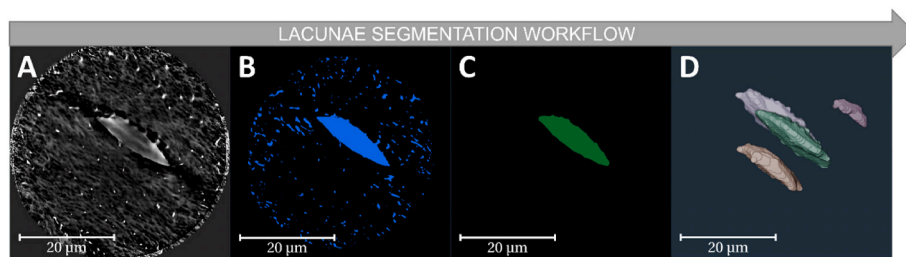

Fig. 3. Sample data workflow of lacunae segmentation in Avizo. A) Denoised TXM image of bone sample showing LCN structures. B) Initial LCN segmentation after greyscale thresholding and manual correction. C) Partially eroded structures with component labelling after smaller volumes are removed. D) Final volume rendering of multiple lacunae after reversing erosion (dilation).
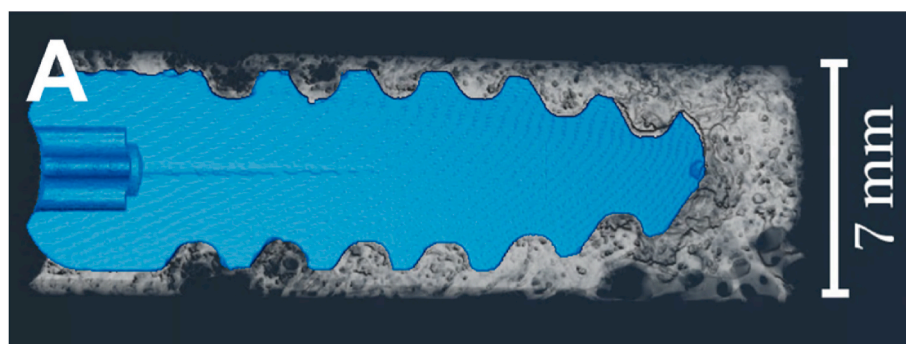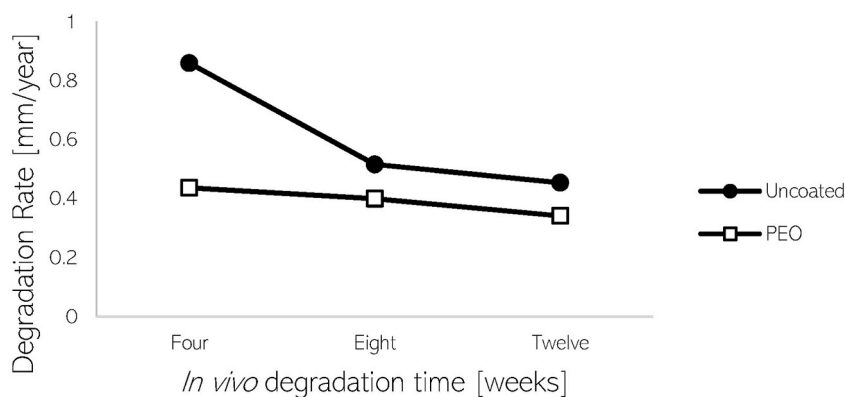
Fig. 4. A) 3D rendering of a 4-week degraded PEO-coated screw surrounded by trabeculae bone created in Avizo. Non-degraded WE43 material is segmented in blue and surrounding non-metallic material in white (bone and degradation layer). B) In vivo degradation rates of uncoated and PEO-coated screws after 4, 8, and 12 weeks calculated from segmented μCT data.
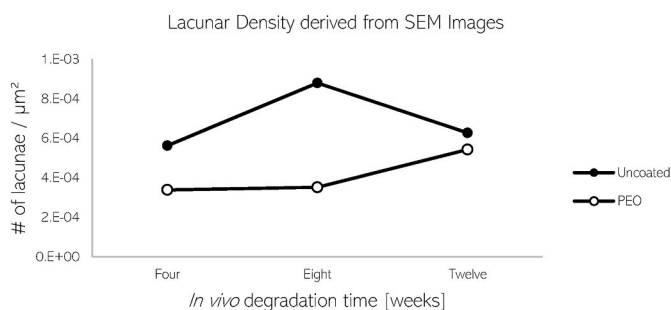

Fig. 5. Calculated lacunar density of uncoated and PEO-coated screws after 4, 8, and 12 weeks calculated from SEM images.

direction seen in the different time points. Thicker and irregular canaliculi are more apparent at 8 weeks of *in vivo* degradation.

3.3. Quantitative analysis of the LCN morphology

Based on the segmented data of the LCN, a quantitative analysis of the network structure was performed. The following figures describe results of the two bone samples found near the implant. Results based on the third sample further from the implant can be found in the Supplementary Material.

Reported values of lacunar porosity and density are depicted in Fig. 7. The lacunar volume in both LCNs found near the implant materials comprises of less than 4% of the total bone volume between four and twelve weeks. From eight to twelve weeks, the lacunar porosity of the LCN surrounding the uncoated material is greater than the selected

LCN near the PEO-coated material. However, an elevated lacunar density near the PEO-coated material is seen during this time period. Bone analysed further away from the uncoated implant revealed a lower average lacunar porosity and density, relative to PEO-coated material.

Lacunar morphology in terms of sphericity and smoothness were investigated for the segmented lacunae. Two general classifications of shapes were found in the bone specimen: smooth and irregular. The lacunae were averaged for each time-point and plotted in Fig. 8. The lacunae found near the PEO-coated implant exhibited a smoother and ellipsoid-like shape in contrast to the irregular-shaped lacunae found near the uncoated material at the analysed time points. Lacunae analysed further away from the implant surface overall display a round and healthy lacunar shape during early time points and decline in smoothness and regularity towards shapes found near the implant as time progresses.

In terms of canalicular structures, the porosity and average number of canaliculi per area of lacunae found near the implant surface are described in Fig. 9. During all time-points, the canaliculi made up a higher percentage of the total bone volume found near the uncoated material, with maximum values at eight weeks. Additionally, a lower number of canaliculi were found attached to lacunae near the PEO implant. With regards to the bone samples further from the implant surface, the canicular presence in terms of porosity and number of canaliculi per area of lacunae was elevated in the bone implanted with uncoated material.

The canalicular junction density and overall LCN porosity of the bone samples located near the implant are shown in Fig. 9. During all observed time-points, the canalicular junction density was elevated in the LCN found near the uncoated material, climaxing at 8 weeks. The total volume of the LCN found around the PEO-coated material was
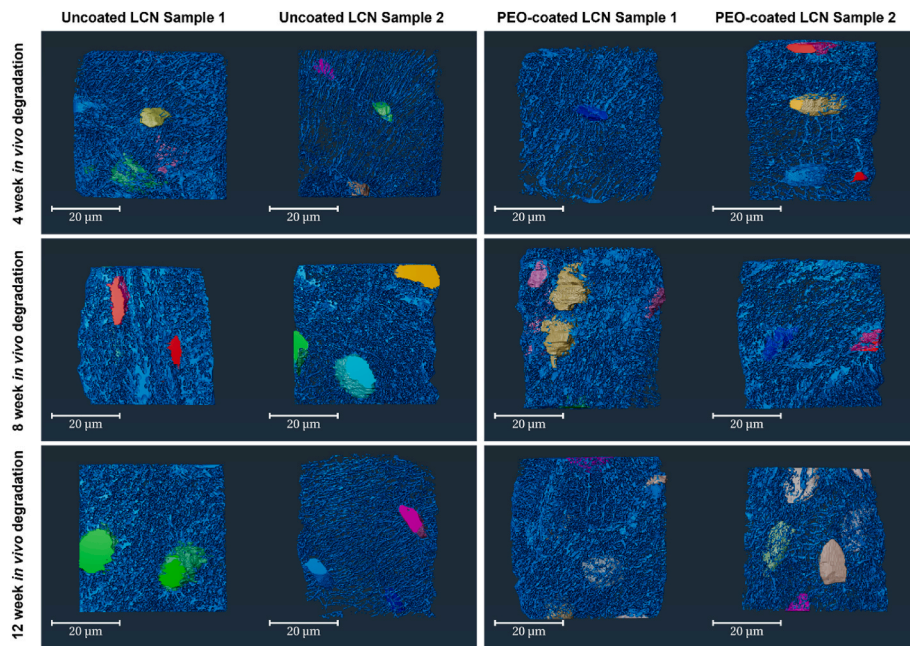
Fig. 6. 3D renderings of the LCN in sheep bone near uncoated and PEO-coated WE43 implants organised by *in vivo* degradation time and material. Renderings were segmented in Avizo highlighting lacunae (colors are for visualization purposes only) and the canaliculi (light blue) for bone specimen after 4, 8, and 12 weeks. Two samples per material were selected for each time-point.
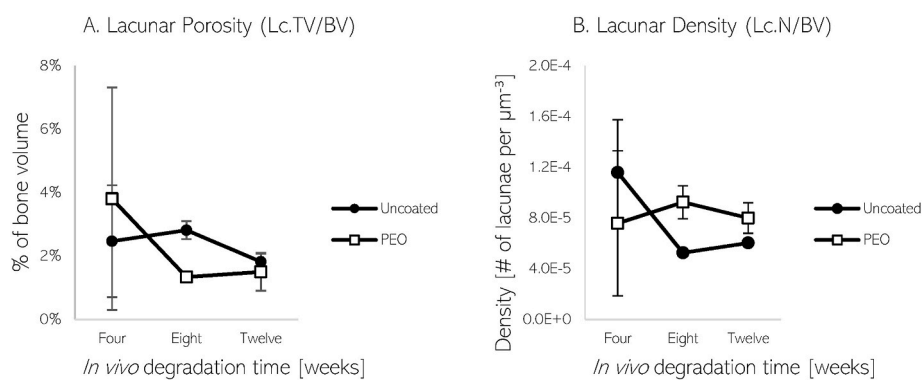

Fig. 7. Plots of lacunar porosity or percentage of lacunar volume in bone (A) and lacunar density (B) of LCN near uncoated and PEO-coated Mg implants after 4, 8, and 12 weeks.
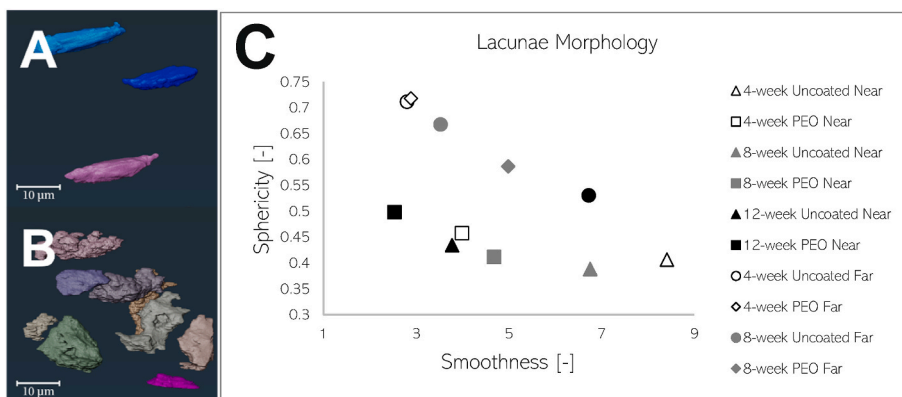

Fig. 8. *3D renderings of sheep lacunae found at 12 weeks (A) and 4 weeks (B) near non-coated WE43 screw samples. Plot (C) describes the average morphology of lacunae found in the LCN near and further away uncoated and PEO-coated WE43 implants in sheep bone. The x-axis describes smoothness or compactness (unitless) of lacunae shape, where a value of 0 corresponds to perfect smoothness. The y-axis describes the sphericity (unitless) of the lacunae shape, where a value of 1 corresponds to a perfect sphere. Samples "near" the implant were selected mms from implant surface, while "far" samples were selected further from the implant surface from undisturbed bone.*

observed to be generally lower. At further distances, the canicular junction density was found to be greater in the bone implanted with non-coated material, but still lower in overall LCN porosity when compared to PEO-coated implanted material.

As a measure of LCN functionality, its transport efficiency can be assessed. Kollmannsberger et al. describe transport efficiency as the time
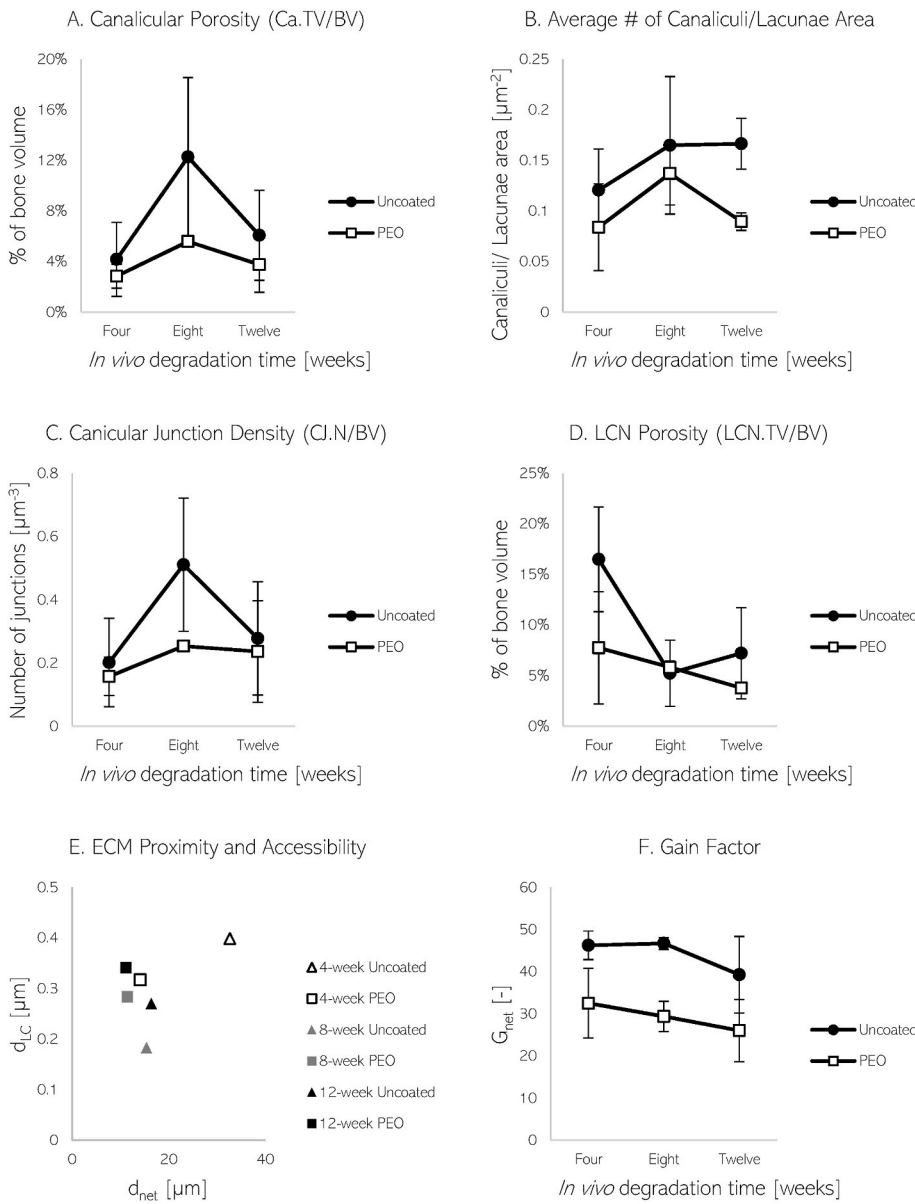
Fig. 9. Plots of canaliculi porosity or percentage of canalicular volume in bone (A), average number of canaliculi per area of lacunae (B), canalicular junction density (C), and LCN porosity or volume (D) near uncoated and PEO-coated WE43 implant material after 4, 8, and 12 weeks. Additionally, the ECM proximity, accessibility (E) and gain factors (F) of bone near uncoated and PEO-coated WE43 implants over time are shown. Parameters d_{LC} denotes LCN distance to matrix voxel, d_{net} denotes average canalicular distance to neighbouring lacunae, and G_{net} is the gain factor.

required for ECF to travel between the osteocytes and ECM, with the assumption that time is proportional to distance. The transport efficiency between the osteocytes and ECM due to the LCN can be described by the gain factor, G_{net} [7]:

$$G_{net} = \frac{d_{LC} + d_{net}}{d_{LC} + \frac{1}{k} \times d_{net}}$$

It is determined by calculating the average 3D Euclidean distance between the LCN and an ECM voxel (d_{LC}), and the average longest distance within the canaliculi to reach the nearest lacunae (d_{net}) where k is the ratio of $v_{network}/v_{matrix}$. A value of $k = 100$ was chosen since the diffusion coefficient of small molecules through bone matrix is approximated to be at least 100 times smaller than for diffusion through the LCN, as described by Kollmannsberger et al. [7].

The LCN near the implant surface of both materials show similar average distances from the ECM (Fig. 9, E). However, there is a much larger variability in ECM proximity and accessibility in terms of d_{LC} and d_{net} seen in the LCN near uncoated samples. The calculated gain factors of the material over the specified time points are shown in Fig. 9 (F). Both materials depict a downward trend in gain factor as time persists.

However, the uncoated material exhibiting higher gain overall. No clear differences between the different implant material were noticed in the ECM proximity of bone further away from the implants. However, the d_{net} was shorter in comparison to bone analysed by the implant. Moreover, the bone further away produced lower Gain Factors when compared to the bone analysed near the implant.

4. Discussion

In this investigation, we report the application of TXM to characterise the LCN morphology of woven sheep bone in the vicinity of implanted biodegradable material for the first time. As discussed, the reactive nature of Mg may lead to rapid degradation rates which do not allow for proper tissue healing, causing overall clinical implication.

As implant degradation occurs, mechanical loading on the implant and surrounding tissue changes as the base metallic material decreases. The rate in which the implant degrades determines how the mechanical loading is distributed throughout the ECM at a specific time, and in turn the shear stress of fluid flow within the LCN from loading. Additionally, the varying degradation rates result in different chemical stimuli sensed

by the osteocytes which may also influence LCN morphology. From our μCT data, a 32% decrease in average degradation rate is exhibited over the selected time points in uncoated samples. This decrease is seemingly low, however, since PEO-coatings have exhibited a reduction in degradation rates by up to 90% and show generally lower degradation rates [58]. With a slower degradation rate introduced by PEO, geometries requiring more material may be produced without risk of premature degradation, such as plates and corresponding screws [23]. Additionally, with a slight increase in implant diameter created by the PEO process described in the methodology, implant stability may improve [59].

Based on SEM imaging, we were able to calculate the lacunar density within 1 mm of the implant material. A higher lacunar density, which has demonstrated to increase nutrients exchange [9], was observed around the uncoated material. An increased lacunar density may have developed as a response to the faster degradation of the uncoated material. With rapid degradation of the uncoated material, a higher amount of nutrients may need to be extracted from the ECM and transported via ECF to initiate bone remodelling processes. As such, the higher lacunar density found around the uncoated material may be aiding in such processes, which may yet to be sensed by the bone surrounding the slower degrading PEO-coated material.

Lacunar morphology has previously been investigated to characterise bone diseases [10–12]. From Fig. 8, a greater portion of imaged lacunae surrounding the PEO material is plotted near the top-left quadrant of the graph, describing the lacunae as rounder and smooth. In comparison, the lacunae surrounding the uncoated material was plotted on the right half of the graph due to their irregularity in shape. The smoother ellipsoidal lacunar shapes found in bone surrounding the PEO-coated material could suggest that lower degradation rates favour lacunar ellipsoidicity. As a result, bone remodelled around the PEO-coated material might be more resistant to micro-damage and micro-cracks as investigated by Liu et al. [34]. Furthermore, smooth ellipse lacunar shapes were determined to be more prominent in mature bone post-operations [60]. With regards to the influence of time, both coated and uncoated bone samples near the implant begin to increase in smoothness as time persists. In contrast, lacunae located further from the implant surface shared smoothness and roundness with that of undisturbed lacunae shape at earlier time points. As time persisted however, the further lacunae begin to increase in irregularity, as seen in Fig. 8c, which may be suggestive of the distance influence between lacunae and implant surface. Regarding lacunar density, a higher number of lacunae in bone is found near the PEO-coated sample after eight weeks. A slower degradation of material caused by the PEO-coating may in turn promote higher density of lacunae. A denser lacunar count might indicate a higher exchange rate of nutrients between the ECF and ECM at lacunar sites, as suggested by Hesse et al. [9].

We found a greater interconnectivity and canalicular presence in the LCN is seen near the uncoated WE43. Furthermore, canalicular porosity and CJ density were higher during all time points, peaking at eight-weeks of degradation. The higher canalicular presence, interconnectivity and higher variability in ECM proximity and accessibility may be indicative of the LCN response to higher degradation rates. Although in our results a higher gain factor may be associated with higher canalicular interconnectivity in our findings, previous studies have found contrary results. Structural quantification of the LCN found in ovine bone has only been documented once in literature. Kollmannsberger et al. analysed the healthy LCN of different mice and sheep bones regarding intercellular transport and communication during a single time-point [7]. The slower-growing sheep bone was found to have lower interconnectivity, however, better organised when compared to the irregular fast-growing mouse bone. By visual inspection, the sheep bone exhibited regular spacing unlike the irregular mouse bone. The analysis revealed a denser canalicular network in sheep bone, greater access to ECM, and gain factors almost double the amount in the mouse bone. However, the study was conducted using confocal microscopy

with voxel sizes of only 200 nm, which may have been a leading cause for the sparse network observed in mice as indicated by the study by Yu et al. which showed that high spatial resolution is required for the most accurate results [3].

When considering the bone samples selected further away from the implant surface, there is a lower canalicular presence and connectivity when compared to bone samples near the implant. In conjunction, the Gain Factor of bone further from the implant was determined to be lower than bone located closer to the implant surface. Casanova et al. have described a progressive increase in connectivity of the LCN during fracture healing in mice during early stages of repair [60], which does not seem to be present at the bone samples further from the implant surface. The lower transportation efficiency and network connectivity observed in distant bone analysed in this investigation may be inherent to undisturbed LCN. The LCN found further away from the implant may not be required to respond to chemical changes caused by the implant material, and therefore display a lack of additional network efficiency and connectivity.

As mentioned, the study led by Kollmannsberger et al. is the only instance in which the LCN is investigated in sheep bone in literature [7]. Kollmannsberger et al. reported a lacunar porosity (or void fraction) of approximately 5 %, which similarly aligns with the lacunar porosity found near the PEO-coated material (4–8 %) in this study. However, canalicular densities in terms of distance per volume reported in our investigation (0.82–2.41 $\mu m/\mu m^3$) are much higher than what is stated by Kollmannsberger et al. (0.19 $\mu m/\mu m^3$). The higher density of the canaliculi observed in our study however, is clearly supported by the segmentation of the canaliculi as visualised in Fig. 6. The distance from a matrix voxel to the LCN (d_{LC}) was found to be smaller in our investigation (0.2–0.4 μm) when compared to the 1 μm reported by Kollmannsberger et al. which again may likely be due to the higher resolution used for imaging in our study. The average distance within the canaliculi to reach a cell body (d_{net}) reported by Kollmannsberger et al. (10.25 μm) more similarly resembled the LCN found near the PEO-coated material (12.25 μm). From our results, the LCN found near the PEO-coated material contributed to a lower gain factor over the analysed time, which more comparably aligns to the reported gain factor of 10 found in mature sheep bone mentioned by Kollmannsberger et al. This may suggest that the slower degradation induced by the PEO-coated material may arrange an LCN with comparable gain capabilities as mature bone. Overall, our quantitative results are in good agreement with the values reported by Kollmannsberger et al.

The LCN is crucial to bone remodelling and maintaining mineral homeostasis. From Fig. 9, we see that bone surrounding the PEO-coated material exhibited lower canalicular porosity and fewer canaliculi attached to the lacunar surfaces when compared to bone found near the uncoated material. The reduced shear stresses sensed by local osteocytes caused by a delayed degradation of metallic base materials may in turn reduce the required permeability of the LCN. Bortel et al. found that interconnectivity between canaliculi promotes robust network transport capabilities and mineral access when canaliculi are interrupted [43]. The study revealed that although interconnectivity increases total canalicular network length, an increase in canaliculi acts to stabilise the overall network performance. If interruption occurs at one pathway, a larger ECM volume is still accessible due to extra connections within the system. Thus, the LCN surrounding the PEO-coated material may have limited access to ECM if canalicular interruption occurs when compared to bone with more connectivity as a response to higher degradation rates. Interestingly, not only is there a stronger canalicular presence near bone found in the vicinity of the implant surface for the uncoated samples, but results from distant bone demonstrate a higher connectivity when compared to bone implanted with PEO-coated material as well.

In addition to earlier works describing the analysis of lacunae and canaliculi, Wittig et al. have introduced a third LCN structure, the canalicular junction (CJ). Findings from their study suggest that these

CJs are integral to osteocyte communication and possibly canalicular ECF flow. We report CJ density values of approximately 10^8 per mm^3 (Fig. 9) and lacunar densities of approximately and 10^4 per mm^3 (Fig. 7) for both implant materials. This factor of 10^4 between CJ and lacunar density may be introduced as response to altered chemical stimuli by the LCN specifically after material implantation, unlike typical stimuli sensed from everyday physical activity. This factor may be characteristic to healing bone as previous studies show a similar quantitative amounts between CJ and lacunar density in healthy bone [6]. Wittig et al. demonstrated that CJs found in healthy sheep femora occur at a density similar to that of osteocyte lacunae. By visual inspection of the segmented TXM data, it is evident that the LCN in our samples are not as evenly dispersed and well-organised as the undisturbed bone specimen imaged by Wittig et al. For this reason, altered stimuli received by the LCN due to implanted material may induce an increase in CJ density. Specifically, a higher degradation rate, as found in the uncoated material, may induce an increase in CJ density in surrounding bone.

This investigation has some limitations. Though LCN variations are apparent between the two materials, statistical analyses could not be performed due to low number of samples. Additionally, the bone sample furthest from the 12-week PEO coated specimen was lost during the manufacturing of the bone specimen. A variability is introduced since bone healing may progress at different speeds depending on the animal, thus requiring an increase in animal samples to better substantiate the results. Furthermore, bone specimen analysed in this investigation were collected from internal woven bone of sheep femur and tibia. Investigations of the superficial lamellar bone response would provide further insight since woven bone is characterised as inadequately organised and less dense with higher cellularity when compared to lamellar bone. The inclusion of longer time points, particular to the PEO-coated material, would provide a deeper understanding and quantification of the delayed effect caused by retarded degradation. Moreover, similar investigations to include human bone is warranted to further justify LCN equivalencies to sheep bone. Surface morphology of the PEO coating should additionally be investigated to determine the influence of implant surface on the LCN.

5. Conclusion

To the best of our knowledge, this pilot investigation is the first of its kind to analyse LCN morphology surrounding a biodegradable implant. Morphological differences in sheep bone LCN have been observed as a response to varied chemical stimuli induced by uncoated and PEO-coated WE43 materials. Smoother ellipsoidal lacunar shapes surrounding PEO-coatings may indicate that lower degradation rates favour lacunae which are better resistant to damage. To the contrary, uncoated material exhibiting higher degradation rates seem to elicit a higher interconnected LCN prone to better stability against canalicular interruption. To confirm delayed variations, PEO-coatings cause on the LCN, similar studies including additional samples, longer time periods, and new complexity measures should further be performed.

Funding sources

CRediT authorship contribution statement

Jonathan Espiritu: Data curation, Formal analysis, Investigation, Methodology, Validation, Visualization, Roles, Writing – original draft. **Sandra Sefa:** Data curation. **Hanna Cwieka:** Data curation. **Imke Greving:** Methodology, Resources, Software, Supervision, Validation, Writing – review & editing. **Silja Flenner:** Funding acquisition, Methodology, Software, Validation, Writing – review & editing. **Regine Willumeit-Römer:** Funding acquisition, Project administration, Writing – review & editing. **Jan-Marten Seitz:** Funding acquisition, Project administration, Resources, Writing – review & editing. **Berit Zeller-Plumhoff:** Conceptualization, Data curation, Investigation, Methodology, Project administration, Software, Supervision, Validation, Writing – review & editing.

Declaration of competing interest

Acknowledgements

Appendix A. Supplementary data

Supplementary data to this article can be found online at https://doi.org/10.1016/j.bioactmat.2023.02.018.

References

[1] D. Krüger, S. Galli, B. Zeller-Plumhoff, D. Wieland, N. Peruzzi, B. Wiese, P. Heuser, J. Moosmann, A. Wennerberg, R. Willumeit-Römer, High-resolution ex vivo analysis of the degradation and osseointegration of Mg-xGd implant screws in 3D, Bioact. Mater. 13 (2022) 37–52.

[2] J. Moosmann, B. Zeller-Plumhoff, D. Wieland, S. Galli, D. Krüger, T. Dose, H. Burmester, F. Wilde, M. Bech, N. Peruzzi, B. Wiese, A. Hipp, F. Beckmann, J. Hammel, R. Willumeit-Römer, Biodegradable magnesium-based implants in bone studied by synchrotron radiation microtomography, in: Proceedings SPIE 10391, Developments in X-Ray Tomography XI, 2017. San Diego, California, US.

[3] B. Yu, A. Pacureanu, C. Olivier, P. Cloetens, F. Peyrin, Assessment of the human bone lacuno-canalicular network at the nanoscale and impact of spatial resolution, Sci. Rep. 10 (2020) 4567.

[4] L. Bonewald, The amazing osteocyte, J. Bone Miner. Res. 26 (2) (2011) 229–238.

[5] F. Shah, P. Thomesen, A. Palmquist, A review of the impact of implant biomaterials on osteocytes, J. Dent. Res. 97 (9) (2018).

[6] N. Wittig, M. Laugesen, M.B.-G.F. Birkbak, A. Pacureanu, S. Bruns, M. Wendelboe, A. Burüel, H. Sorenson, J.B.H. Thomsen, Canalicular junctions in the osteocyte lacuno-canalicular network of cortical bone, ACS Nano 13 (6) (2019) 6421–6430.

[7] P. Kollmannsberger, M. Kerschnitzki, F. Repp, W. Wagermaier, R. Weinkamer, P. Fratzl, The small world of osteocytes: connectomics of the lacuno-canalicular network in bone, New J. Phys. 19 (2017).

[8] J. Wang, F. Jia, T. Gilbert, S. Woo, Cell orientation determines the alignment of cell-produced collagenous matrix, J. Biomech. 36 (1) (2003) 97–102.

[9] B. Hesse, P. Varga, M. Langer, A. Pacureanu, S. Schrof, N. Männicke, H. Suhonen, P. Maurer, P. Cloetens, F. Peyrin, K. Raum, Canalicular network morphology is the major determinant of the spatial distribution of mass density in human bone tissue: evidence by means of synchrotron radiation phase-contrast nano-CT, J. Bone Miner. Res. 30 (2) (2014) 346–356.

[10] A. Ashique, L. Hart, C. Thomas, J. Clement, P. Pivonka, Y. Carter, D. Mousseau, D. Cooper, Lacunar-canalicular network in femoral cortical bone is reduced in aged women and is predominantly due to a loss of canalicular porosity, BoneKEy Rep. 7 (2017) 9–16.

[11] M. Tate, J. Adamson, A. Tami, T. Bauer, The osteocyte, Int. J. Biochem. Cell Biol. 36 (1) (2004) 1–8.

[12] L. Tiede-Lewis, S. Dallas, Changes in the osteocyte lacunocanalicular network with aging, Bone 112 (2019) 101–113.

[13] M. Hussein, A. Mohammed, N. Al-Aqeeli, Wear characteristics of metallic biomaterials: a review, Materials 8 (5) (2015) 2749–2768.

[14] D. Vos, M. Verhofstad, Indications for implant removal after fracture healing: a review of the literature, Eur. J. Trauma Emerg. Surg. 39 (2013) 327–337.

[15] H. Windhagen, K.W.A. Radtke, J. Diekmann, Y. Noll, U. Kreimeyer, R. Schavan, C. Stukenborg-Colsman, H. Waizy, Biodegradable magnesium-based screw clinically equivalent to titanium screw in hallux valgus surgery: short term results of the first prospective, randomized, controlled clinical pilot study, Biomed. Eng. Online 12 (62) (2013).

[16] H. Zhou, B. Liang, H. Jiang, Z. Deng, K. Yu, Magnesium-based biomaterials as emerging agents for bone repair and regeneration: from mechanism to application, Journal of Magnesium and Alloys 9 (3) (2021) 779–804.

[17] S. Amukarimi, M. Mozafari, Biodegradable magnesium-based biomaterials: an overview of challenges and opportunities, MedComm 2 (2) (2021) 123–144.

[18] H. May, Y. Kati, G. Gumussuyu, T. Emre, M. Unal, O. Kose, Bioabsorbable magnesium screw versus conventional titanium screw fixation for medial malleolar fractures, J. Orthop. Traumatol. 21 (9) (2020).

[19] F. Wagner, A. Post, T. Yilmaz, D. Maier, J. Neubauer, M. Feucht, N. Südkamp, K. Reising, Biomechanical comparison of biodegradable magnesium screws and titanium screws for operative stabilization of displaced capitellar fractures, J. Shoulder Elbow Surg. 29 (9) (2020) 1912–1919.

[20] B. Acar, O. Kose, M. Unal, A. Turan, Y. Kati, F. Guler, Comparison of magnesium versus titanium screw fixation for biplane chevron medial malleolar osteotomy in the treatment of osteochondral lesions of the talus, Eur. J. Orthop. Surg. Traumatol. 30 (2020) 163–173.

[21] H. Atkinson, S. Khan, Y. Lashgari, A. Ziegler, Hallux valgus correction utilising a modified short scarf osteotomy with a magnesium biodegradable or titanium compression screws – a comparative study of clinical outcomes, BMC Muscoskel. Disord. 20 (334) (2019).

[22] B. Acar, O. Kose, A. Turan, M. Unal, Y. Kati, F. Guler, Comparison of bioabsorbable magnesium versus titanium screw fixation for modified distal chevron osteotomy in hallux valgus, BioMed Res. Int. 2018 (2018) 9.

[23] C. Rendenbach, H. Fischer, A. Kopp, K. Schmidt-Bleek, H. Kreiker, S. Stumpp, M. Thiele, G. Duda, H. Hanken, B. Beck-Broichsitter, O. Jung, N. Kröger, R. Smeets, M. Heiland, Improved in vivo osseointegration and degradation behavior of PEO surface-modified WE43 magnesium plates and screws after 6 and 12 months, Mater. Sci. Eng. C 129 (2021).

[24] H. Sampatirao, S. Radhakrishnapillai, S. Dondapati, E. Parfenov, R. Nagumothu, Developments in plasma electrolytic oxidation (PEO) coatings for biodegradable magnesium alloys, Mater. Today Proc. 46 (2) (2021) 1407–1415.

[25] T. Monetta, P. Parnian, A. Acquesta, Recent advances in the control of the degradation rate of PEO treated magnesium and its alloys for biomedical applications, Metals 10 (7) (2020).

[26] E. Matykina, I. Garcia, R. Arrabal, M. Mohedano, B. Mingo, J. Sancho, M. Merino, A. Pardo, Role of PEO coatings in long-term biodegradation of a Mg alloy, Appl. Surf. Sci. 389 (2016) 810–823.

[27] H. Sampatirao, S. Radhakrishnapillai, S. Dondapati, E. Parfenov, R. Nagumothu, Developments in plasma electrolytic oxidation (PEO) coatings for biodegradable magnesium alloys, Materials Stoday; Proceedings 46 (2) (2021) 1407–1415.

[28] F. Shah, X. Wang, P. Thomsen, K. Grandfield, A. Palmquist, High-resolution visualization of the osteocyte lacuno-canalicular network juxtaposed to the surface of nanotextured titanium implants in human, ACS Biomater. Sci. Eng. 1 (5) (2015) 305–313.

[29] T. Nakashima, M. Hayashi, T. Fukunaga, K. Kurata, M. Oh-hora, J. Feng, L. Bonewald, T. Kodama, A. Wutz, E. Wagner, J.T.H. Penninger, Evidence for osteocyte regulation of bone homeostasis through RANKL expression, Nat. Med. 17 (2011) 1231–1234.

[30] L. You, S. Weinbaum, S. Cowin, M. Schaffler, Ultrastructure of the osteocyte process and its pericellular matrix, Anat. Rec. 278A (2) (2004) 505–513.

[31] Y. Lin, S. Xu, AFM analysis of the lacunar-canalicular network in demineralized compact bone, J. Microsc. 241 (3) (2010) 291–302.

[32] S. Hirose, M. Li, T. Kojima, P. de Freitas, S. Ubaidus, K. Oda, C. Saito, N. Amizuka, A histological assessment on the distribution of the osteocytic lacunar canalicular system using silver staining, J. Bone Miner. Metabol. 25 (2007) 374–382.

[33] T. Hasegawa, T. Yamamoto, H. Hongo, Z. Qiu, M. Abe, T. Kanesaki, K. Tanaka, T. Endo, P. de Freitas, M. Li, N. Amizuka, Three-dimensional ultrastructure of osteocytes assessed by focused ion beam-scanning electron microscopy (FIB-SEM), Histochem. Cell Biol. 149 (2018) 423–432.

[34] Y. Liu, B. Chen, D. Yin, Effects of direction and shape of osteocyte lacunae on resisting impact and micro-damage of osteon, J. Mater. Sci. Mater. Med. 28 (38) (2017).

[35] P. Schneider, M. Meier, R. Wepf, R. Müller, Serial FIB/SEM imaging for quantitative 3D assessment of the osteocyte lacuno-canalicular network, Bone 49 (2) (2011) 304–311.

[36] S. Okada, S. Yoshida, S. Ashrafi, D. Schraufnagel, The canalicular structure of compact bone in the rat at different ages, Microsc. Microanal. 8 (2) (2002) 104–115.

[37] H. Kamioka, Y. Kameo, Y. Imai, A. Bakker, R. Bacabac, N. Yamada, A. Takaoka, T. Yamashiro, T. Adachi, J. Klein-Nulend, Microscale fluid flow analysis in a human osteocyte canaliculus using a realistic high-resolution image-based three-dimensional model, Integrative Biology 4 (10) (2012) 1198–1206.

[38] H. Kamioka, S. Murshid, Y. Ishihara, N. Kajimura, T. Hasegawa, R. Ando, Y. Sugawara, T. Yamashiro, A. Takaoka, T. Takano-Yamamoto, A method for observing silver-stained osteocytes in situ in 3-μm sections using ultra-high voltage electron microscopy tomography, Microsc. Microanal. 15 (5) (2009) 377–383.

[39] M. Rubin, J. Rubin, I. Jasiuk, SEM and TEM study of the hierarchical structure of C57BL/6J and C3H/HeJ mice trabecular bone, Bone 35 (1) (2004) 11–20.

[40] R. Genthial, E. Beaurepaire, M. Schanne-Klein, F. Peyrin, D. Farlay, C. Olivier, Y. Bala, G. Boivin, J. Vial, D. Debarre, A. Gourrier, Label-free imaging of bone multiscale porosity and interfaces using third-harmonic generation microscopy, Sci. Rep. 7 (2017).

[41] S. Kamel-ElSayed, L. Tiede-Lewis, Y. Lu, P. Veno, S. Dallas, Novel approaches for two and three dimensional multiplexed imaging of osteocytes, Bone 76 (2015) 129–140.

[42] M. Dierolf, A. Menzel, P. Thibault, P. Schneider, C. Kewish, R. Wepf, O. Bunk, F. Pfeiffer, Ptychographic X-ray computed tomography at the nanoscale, Nature 467 (2010) 436–439.

[43] E. Bortel, L. Gover, N. Eisenstein, C. Seim, H. Suhonen, A. Pacureanu, P. Westenberger, K. Raum, M. Langer, F. Peyring, O. Addison, B. Hesse, Interconnectivity explains high canalicular network robustness between neighboring osteocyte lacunae in human bone, Adv. Nano Biomed Res. 2 (4) (2021).

[44] A. Pacureanu, M. Langer, E. Boller, P. Tafforeau, F. Peyrin, Nanoscale imaging of the bone cell network with synchrotron X-ray tomography: optimization of acquisition setup, Med. Phys. 39 (4) (2012) 2229–2238.

[45] P. Varga, B. Hesse, M. Langer, S. Schrof, N. Männicke, H. Suhonen, A. Pacureanu, D. Pahr, F. Peyrin, K. Raum, Synchrotron X-ray phase nano-tomography-based analysis of the lacunar–canalicular network morphology and its relation to the strains experienced by osteocytes in situ as predicted by case-specific finite element analysis, Biomech. Model. Mechanobiol. 14 (2015) 267–282.

[46] E. Stockhausen, M. Qwamizadeh, E. Wölfel, H. Hemmatian, I. Fiedler, S. Flenner, E. Longo, M. Amling, I. Greving, R. Ritchie, F. Schmidt, B. Busse, Collagen fiber orientation is coupled with specific nano-compositional patterns in dark and bright osteons modulating their biomechanical properties, ACS Nano 12 (1) (2021) 455–467.

[47] S. Flenner, A. Kubec, C. David, M. Storm, C. Schaber, F. Vollrath, M. Müller, I. Greving, J. Hagemann, Hard X-ray nano-holotomography with a Fresnel zone plate, Opt Express 28 (25) (2020) 37514–37525.

[48] B. Zeller-Plumhoff, D. Tolnai, M. Wolff, I. Greving, H. Norbert, R. Willumeit-Römer, Utilizing synchrotron radiation for the characterization of biodegradable magnesium alloys—from alloy development to the application as implant material, Adv. Eng. Mater. 23 (11) (2021).

[49] A. Materials, Magnesium Elektron WE43 Alloy (UNS M18430), 2022 [Online]. Available: https://www.azom.com/article.aspx?ArticleID=9279. (Accessed 29 July 2022).

[50] S. Ag, Method for Producing a Medical Implant from a Magnesium Alloy", United States Patent US9402669B2, 2011, 06 09.

[51] I. O. f. S. (ISO), Biological Evaluation of Medical Devices — Part 6: Tests for Local Effects after Implantation, ISO 10993-6:2007, Berlin, Germany, 2007.

[52] S. Flenner, M. Storm, A. Kubec, E. Longo, F. Döring, D. Pelt, C. David, M. Müller, I. Greving, Pushing the temporal resolution in absorption and Zernike phase contrast nanotomography: enabling fast in situ experiments, Jounral of Synchrotron Radiation 27 (5) (2020) 1339–1346.

[53] D. Gürsoy, F. De Carlo, X. Xiao, C. Jacobsen, TomoPy: a framework for the analysis of synchrotron tomographic data, J. Synchrotron Radiat. 21 (5) (2014) 1188–1193.

[54] J. Schindelin, I. Arganda-Carreras, E. Frise, V. Kaynig, M. Longair, T. Pietzsch, S. Preibisch, C. Rueden, S. Saalfeld, B. Schmid, J. Tinevez, D. White, V. Hartenstein, K. Eliceiri, P. Tomancak, A. Cardona, Fiji: an open-source platform for biological-image analysis, Nat. Methods 9 (2012) 676–682.

[55] E. Nidadavolu, F. Feyerabend, T. Ebel, R. Willumeit-Römer, M. Dahms, On the determination of magnesium degradation rates under physiological conditions, Materials 9 (8) (2016) 627.

[56] S. Bruns, S. Stipp, H. Sorensen, Looking for the Signal: a guide to iterative noise and artefact removal in X-ray tomographic reconstructions of porous geomaterials, Adv. Water Resour. 105 (2017) 96–107.

[57] D. Legland, I. Arganda-Carreras, P. Andrey, MorphoLibJ: integrated library and plugins for mathematical morphology with ImageJ, Bioinformatics 32 (22) (2016) 3532–3534.

[58] X. Gu, S. Li, X. Li, Y. Fan, Magnesium based degradable biomaterials: a review, Front. Mater. Sci. 8 (2014) 200–218.

[59] C. Ivanoff, L. Sennerby, C. Johansson, B. Rangert, U. Lekholm, Influence of implant diameters on the integration of screw implants: an experimental study in rabbits, Int. J. Oral Maxillofac. Surg. 26 (2) (1997) 141–148.

[60] M. Casanova, A. Schindeler, L. Peacock, L. Lee, P. Schneider, D. Little, R. Müller, Characterization of the developing lacunocanalicular network during fracture repair, JBMR Plus 5 (9) (2021).